nature biomedical engineering

Supplementary information

https://doi.org/10.1038/s41551-026-01771-y

A miniature endovascular soft robot for active blood flow regulation in occluded vessels

In the format provided by the authors and unedited

Content

Note S1. Design and fabrication of the robot

Design considerations: The magnetic miniature robot is designed to meet multiple needs: endovascular deployment through a catheter, wireless magnetic navigation to the target area, and robotic flow regulation, all monitored by medical imaging. To meet these requirements, it adopts a bilayer design, which includes a magnetic layer and a cilia carpet. The magnetic layer with high NdFeB particle density has a large magnetic moment, which experiences a larger force under magnetic field gradients, thereby enabling efficient intravascular propulsion. The preprogrammed deformation of the magnetic layer under magnetic fields shapes the cilia carpet into a cylinder matching the tubular structure of blood vessels, and the high NdFeB particle density makes the robot clearly visible under X-ray. By coiling the cilia carpet for magnetization (fig. S1 and S4A), the cilia are encoded with magnetization phase shifts and perform metachronal waves, thereby achieving flow regulation. The two layers are respectively magnetized and assembled together, therefore decoupling the magnetization profiles. It enables actuation mode switching by tuning the plane of the rotating magnetic field. Hence, when the robot approaches the target area, the robot can perform robotic flow regulation while maintaining its position, guaranteeing the precision of the entire procedure.

Fabrication methods: The robot employs a PDMS (Polydimethylsiloxane) based matrix to ensure biocompatibility. NdFeB particles are embedded into the PDMS precursor, which is then cured at 60 ℃ and magnetized under a pulsed magnetic field with strength higher than 1.5 T to achieve saturation. This process enhances its net magnetic moment, enabling programmable deformation under external magnetic fields. For assembly, plasma treatment activates the PDMS surfaces, allowing irreversible bonding when the magnetic layer and the cilia carpet are pressed together, ensuring structural integrity.

Note S2. Magnetic actuation of the robot

Locomotion of the robot: When applying a rotating magnetic field by using a magnet, the whole robot will rotate, thereby reducing the friction force with the vessel wall. Meanwhile, when the magnet translates, the robot is dragged by the magnetic force and intravascular locomotion is achieved. The magnetic force F_m acting on the robot under an external magnetic field can be expressed as:

$$F_m = (m \cdot \nabla) B$$

where F_m, m, B denote the magnetic force, the net magnetic moment of the robot, and the applied magnetic field.

Deformation of the cilia: The robot actuation mode can switch from intravascular locomotion to robotic flow regulation by tuning the actuation angle, which is the angle between the magnet rotating axis and the robot movement direction (inset, Fig. 5C). When the magnet rotating axis is perpendicular to the robot movement direction, the rotation of the whole robot is hindered by the vessel wall, and the robot will maintain its position. Instead, only the cilia are actuated, and robotic flow regulation is achieved.

The cilia are fabricated by a composite material combining PDMS and NdFeB particles (see Methods and Note S1). During magnetization, the cilia carpet is coiled for magnetization (fig. S1). The magnetization process induces a nonuniform magnetization profile within the composite material. When the cilia are exposed to an external magnetic field, the magnetized NdFeB particles tend to align with the field direction, generating magnetic torque that drives the structure to deform toward its predefined programmed shape. The magnetic torque is given by:

$$\tau_m = m_c \times B$$

where τ_m, m_c, B denote the magnetic torque, the magnetization of the cilia, and the applied magnetic field.

According to the Euler-Bernoulli equation for beams, the relationship between the magnetic torque and deformation of the magnetic object is given by:

$$\tau_m = EI \cdot \kappa$$

where E, I, κ are the elastic modulus, area moment of inertia, and the curvature of the cilia, respectively.

Note S3. Anchoring stability of the robot

The anchoring stability is governed by the force balance between the friction force $\boldsymbol{f}_s$ and the fluid drag force $\boldsymbol{F}_d$. The friction force can be modeled as:

$$\boldsymbol{f}_s \leq \boldsymbol{f}_{s,max} = \mu_s N = \mu_s\left(\boldsymbol{F}_{elastic} + \boldsymbol{F}_{fluid,radial}\right)$$

where $\boldsymbol{f}_{s,\,max}$, μ_s, N, $\boldsymbol{F}_{elastic}$, $\boldsymbol{F}_{fluid,axial}$ are the maximum static friction force, the coefficient of static friction, the normal force perpendicular to the contact surface, the elastic restoring force of the rolled-up robot pressing against the vessel wall, and the radial component of the hydrodynamic force, respectively.

The fluid drag force $\boldsymbol{F}_d$ is given by:

$$\boldsymbol{F}_d = \frac{1}{2} C_d \rho A v^2$$

In the equation, C_d is the drag coefficient, ρ is the density of blood, A is the cross-sectional area of the object perpendicular to the flow direction, and v is the flow velocity. According to the model, the robot remains anchored to the vessel wall as long as the maximum static friction force $f_{s,\,max}$ exceeds the fluid drag force F_d.

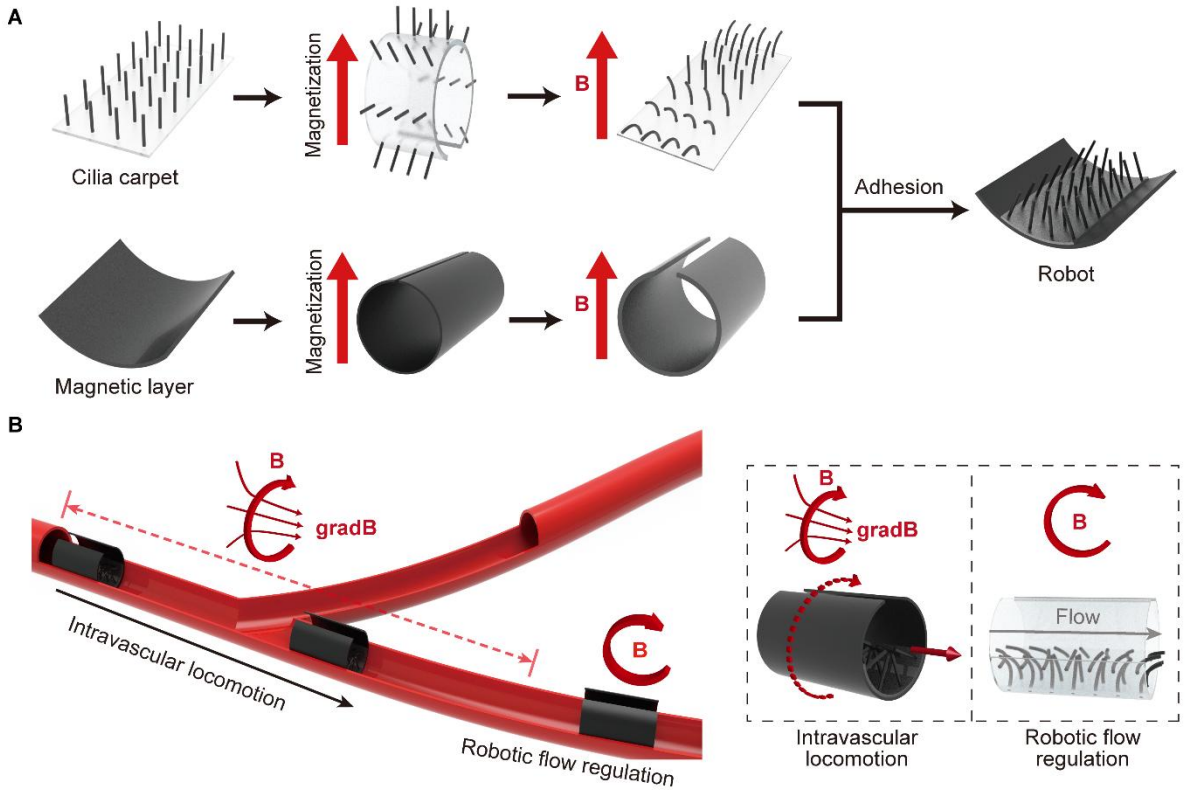

Fig. S1. Fabrication process and actuation modes of the robot. (**A**) Design and fabrication process of the robot. The robot adopts a bilayer design, which is composed of a cilia carpet and a magnetic layer. The cilia carpet and the magnetic layer are magnetized, respectively. After magnetization, the cilia carpet and the magnetic layer are assembled together by plasma treatment. The cilia can generate flow through their non-reciprocal motions and metachronal waves. The magnetic layer provides locomotion ability and enables visibility under medical imaging. (**B**) Actuation modes of the robot. The actuation modes of the robot are decoupled into intravascular locomotion and robotic flow regulation by tuning the magnetic field. Schematic illustrations are created using SolidWorks and Keyshot.

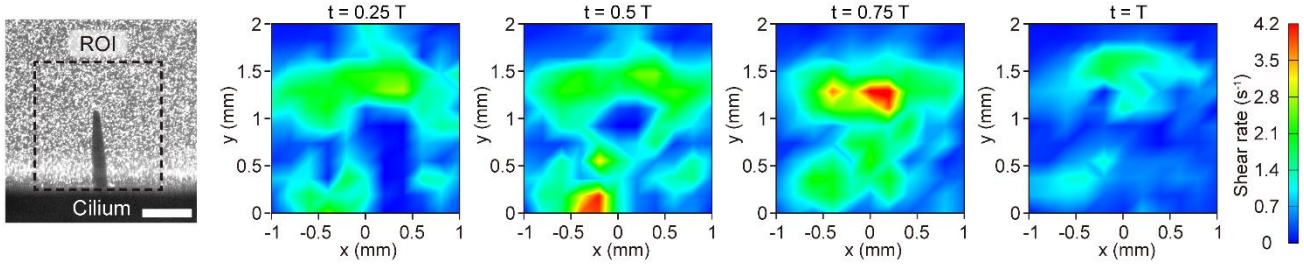

Fig. S2. Characterization of the shear stress induced by a cilium using Particle Image Velocimetry (PIV). The black dashed box indicates the region of interest (ROI) where the flow field is analyzed. The actuation frequency is 20 Hz. Scale bar, 1 mm.

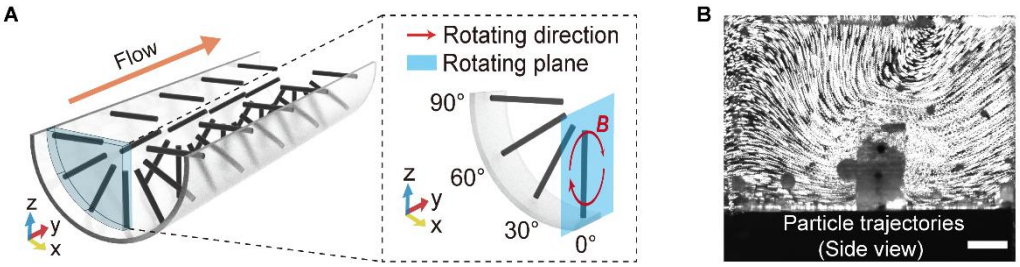

Fig. S3. The analysis of a single cilium and a curled cilia array. (**A**) Schematic of a cilia carpet deployed in a tubular configuration, and each cilium exhibits a field-cilium angle, which is the angle between its long axis and the rotating plane of the magnetic field. (**B**) The flow field generated by a semicircular cilia array visualized by fluorescent tracer particles. Scale bar, 1 mm. Schematic illustrations are created using SolidWorks and Keyshot.

Note S4. Three-dimensional numerical simulation of the flow field

The static magnetic field distribution generated by the NdFeB permanent magnet is simulated by the Magnetic Fields interface in COMSOL Multiphysics under steady-state conditions (fig. S3). The governing equations include the divergence-free condition of the magnetic field flux density, which can be expressed as

$$\nabla \cdot \mathbf{B} = 0$$

where B is the magnetic flux density. This divergence-free condition applies universally to both the magnet and surrounding air domains.

For the NdFeB magnet, the nonlinear remanent flux density model is applied:

$$\mathbf{B} = \mu_0 \mu_{rec} \mathbf{H} + \mathbf{B_r}$$

where μ_{rec} (recoil permeability, anisotropic tensor from the COMSOL material library) and B_r (remanent flux density) defined the hard magnetic properties.

For the air domain, the linear constitutive relation can be expressed as:

$$\mathbf{B} = \mu_0 \mu_r \mathbf{H}$$

where μ_0 is vacuum permeability and μ_r is the relative permeability.

The external boundary of the air domain satisfies：

$$\mathbf{n} \cdot \mathbf{B} = 0$$

where n denotes the unit normal vector to the boundary.

The field solution employs the magnetic scalar potential (V_m) reduction:

$$\mathbf{H} = -\nabla V_m$$

This formulation avoids direct current source terms, consistent with permanent magnet simulations in the absence of external excitation.

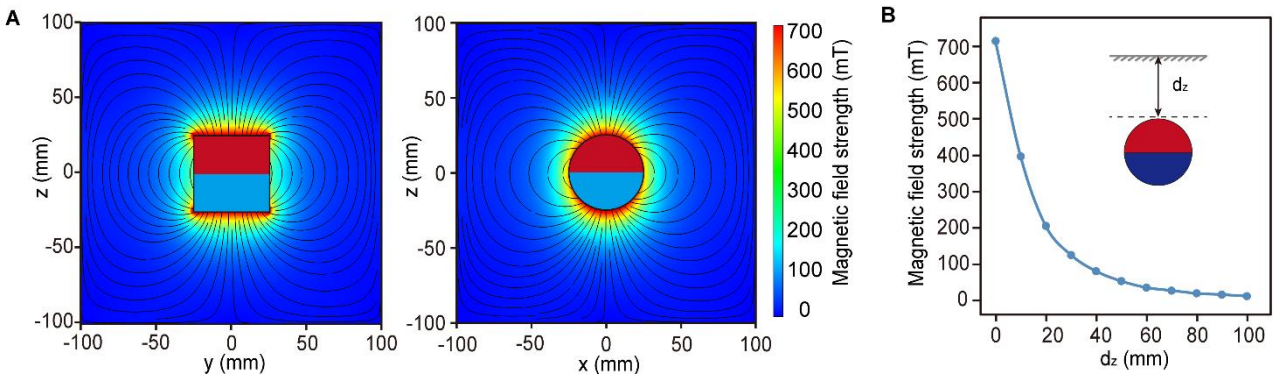

Fig. S4. Simulation and characterization of the cylindrical magnet. (**A**) Three-dimensional numerical simulation of the magnetic field distribution of the cylindrical magnet. (**B**) The relationship between field strength and the distance to the magnet (d_z).

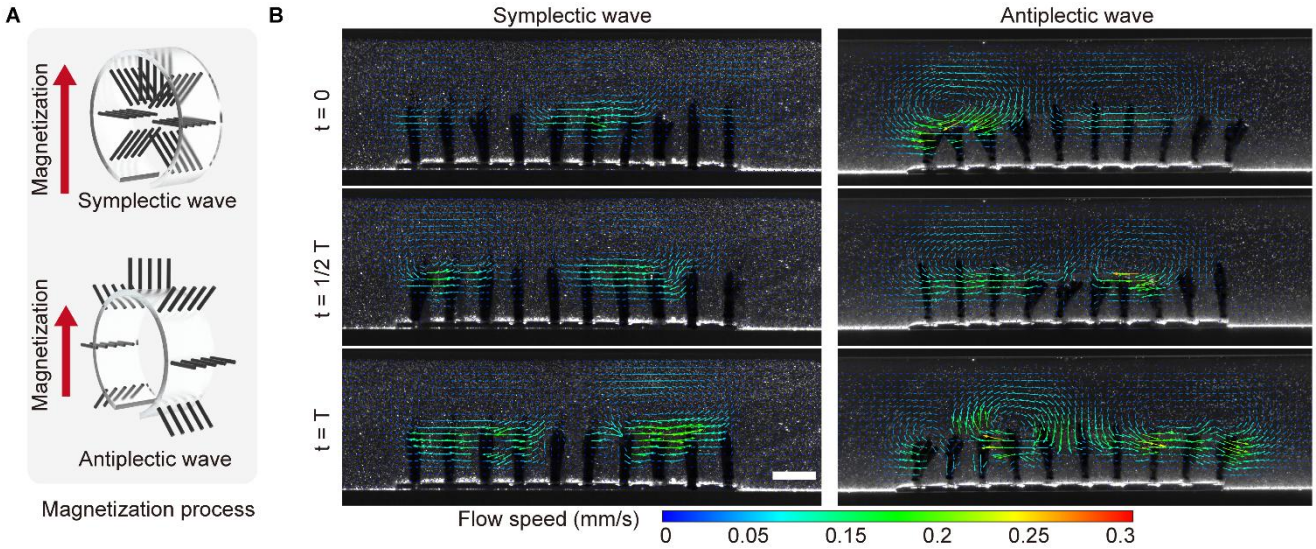

Fig. S5. Analysis of cilia carpets with symplectic and antiplectic waves. (**A**) Magnetization process of cilia carpets with different metachronal waves. (**B**) The transient flow fields generated by cilia carpets with antiplectic and symplectic waves through one cycle. The transient flow fields are analyzed using a PIV system. Scale bar, 1.5 mm. Schematic illustrations are created using SolidWorks and Keyshot.

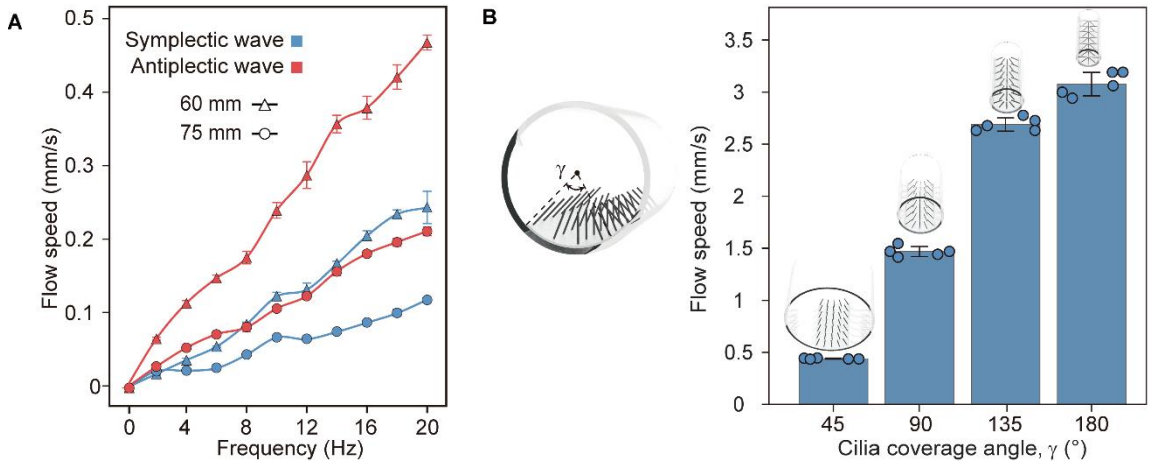

Fig. S6. Flow speed characterization of cilia carpet. (**A**) The change of flow speed with actuation frequency at each actuation distance (60, and 75 mm). The blue and red curves are the speeds of the flow induced by cilia carpets with symplectic and antiplectic waves, respectively. (**B**) The relationship between the flow speed and the cilia coverage angle in vessels with different diameters. The cilia carpet is placed in vessels with different diameters, a larger diameter leads to a smaller cilia coverage angle. The frequency of the magnetic field is 14Hz, and the actuation distance is 45 mm. Data are presented as mean ± s.d. from five technical replicates (n = 5). Schematic illustrations are created using SolidWorks and Keyshot.

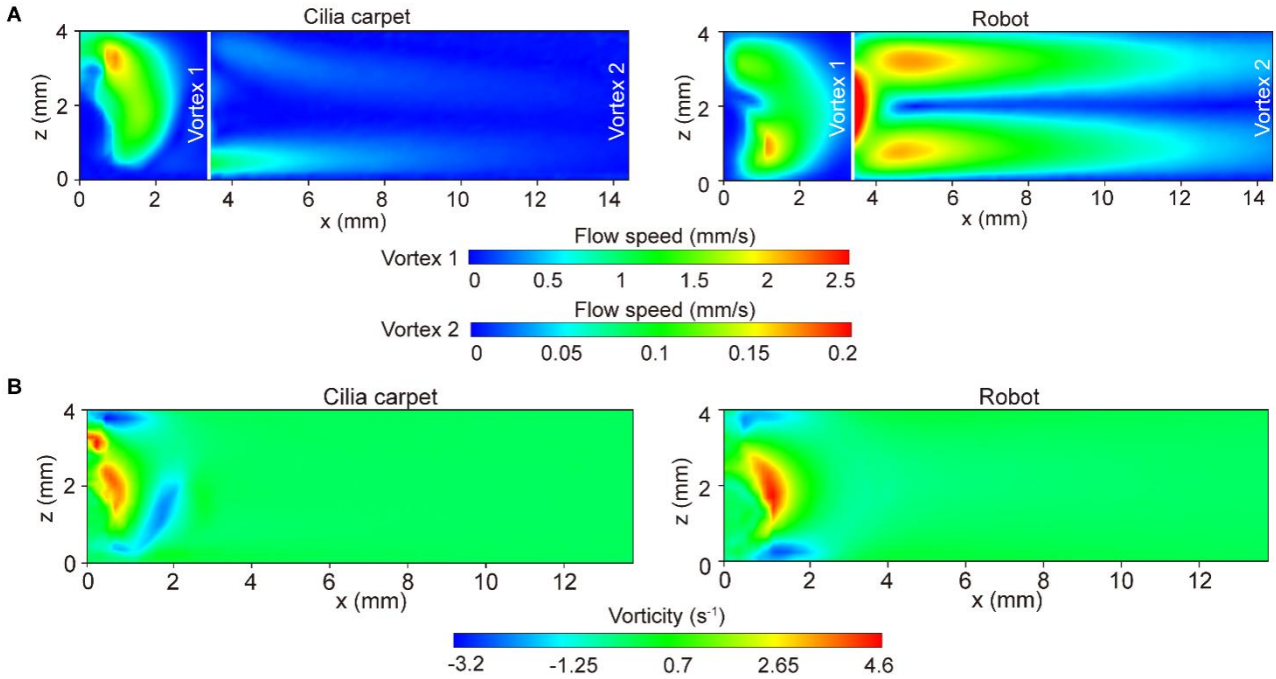

Fig. S7. Comparisons of flow fields in Region 2 induced by the cilia carpet and robot visualized by the PIV system. (**A**) The fluid velocity fields induced by the cilia carpet and the robot in Region 2. (**B**) The vorticity analysis of flow fields induced by the cilia carpet and robot in Region 2.

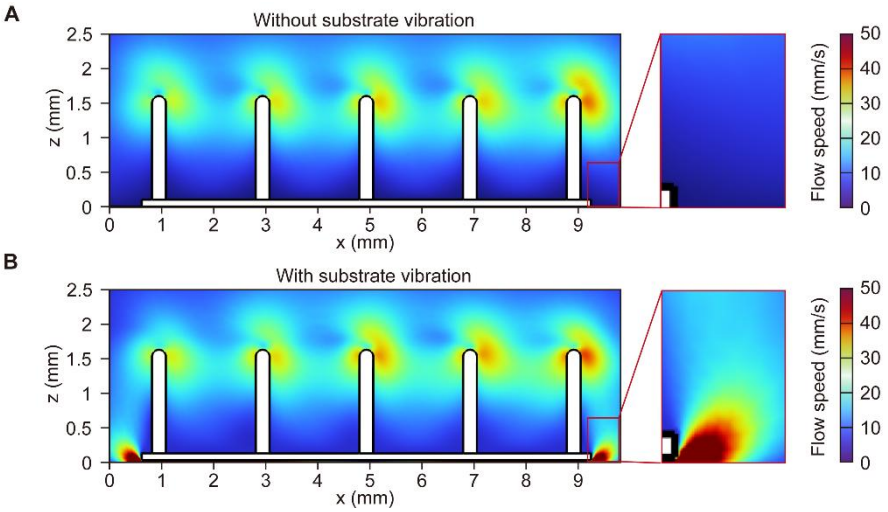

Fig. S8. Simulation of boundary layer disruption induced by substrate vibration. (**A**) Flow field induced by cilia beating on a static substrate. (**B**) Flow field induced by cilia beating on a vibrating substrate. The vibrating amplitude and frequency are 50 μm and 20 Hz, respectively.

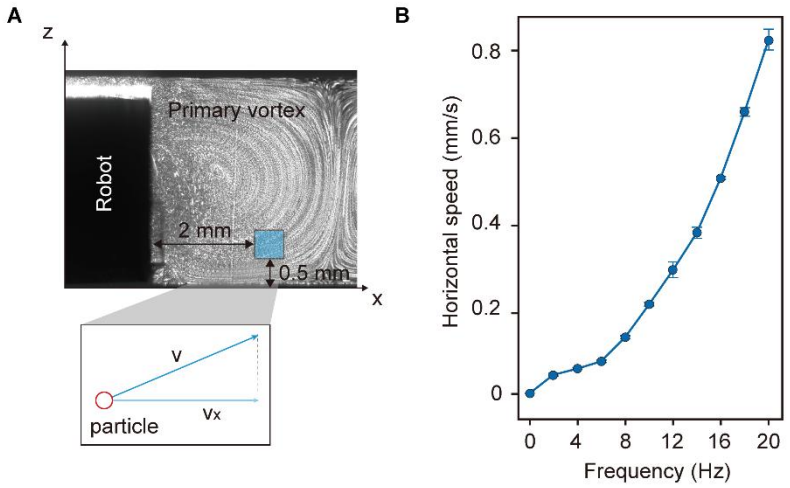

Fig. S9. Characterization of the primary vortex induced by the robot. (**A**) The schematics of the characteristic metric. The strength of the primary vortex is characterized by the horizontal speed component of particles in the sample area. The blue box indicates the sample area. The height and width of the sample area are 0.5 mm. (**B**) The relationship between the particle horizontal speed within the sample area and the actuation frequency. Data are presented as mean ± s.d. from three technical replicates (n = 3).

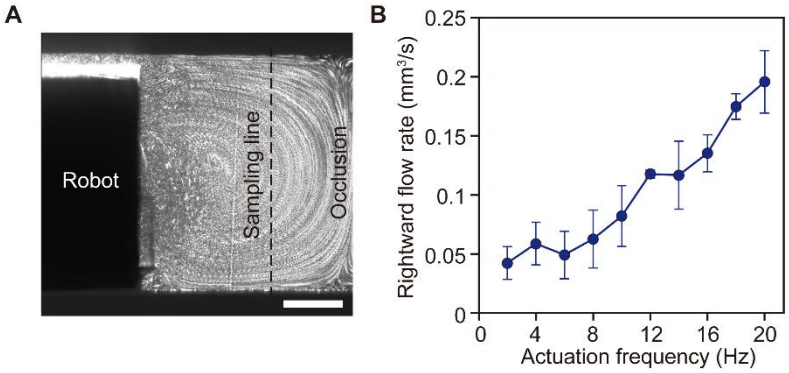

Fig. S10. Characterization of the fluid exchange efficiency of the robot. (**A**) PIV visualization of the flow streamlines generated by the robot, showing the formation of a vortex. A vertical sampling line (dashed line) is defined across the vortex. The fluid exchange efficiency is characterized by the net rightward flow rate passing through this line. Scale bar, 1 mm. (**B**) The relationship between the rightward flow rate across the sampling line and the actuation frequency. The thickness of the sampling is defined as 0.1 mm to get a volumetric flow rate. Data are presented as mean ± s.d. from three independent experiments (n = 3).

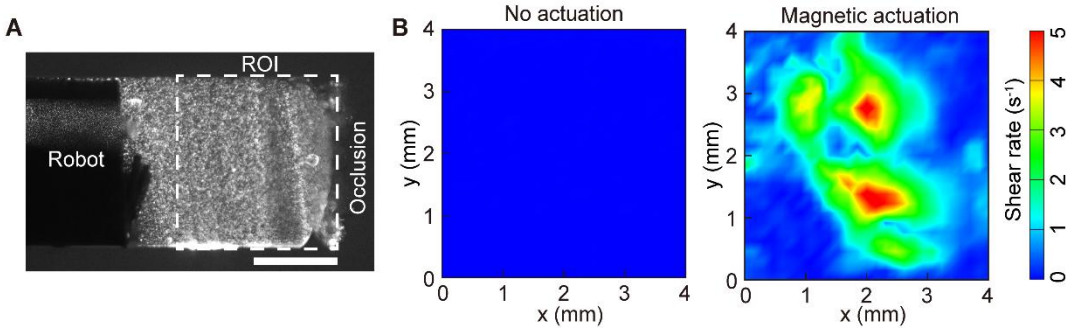

Fig. S11. Characterization of the shear rate induced by the robot using Particle Image Velocimetry (PIV). (**A**) Region of interest for PIV analysis. Scale bar, 2 mm. (**B**) Shear rate distribution with and without robot actuation in the ROI. The actuation frequency is 20 Hz.

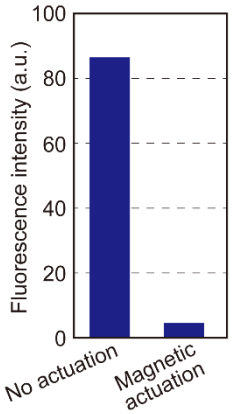

Fig. S12. Fluorescence intensity of the adhered fluorescent particles before and after robot actuation.

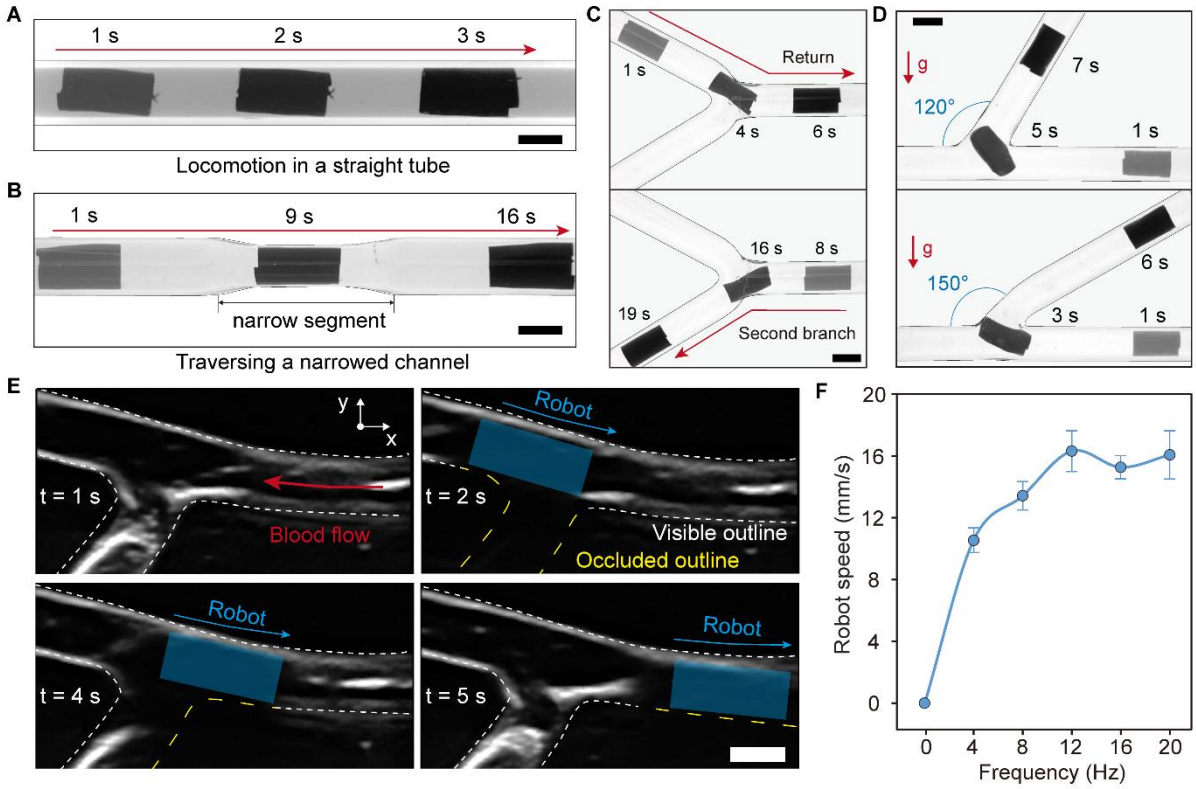

Fig. S13. In vitro locomotion of the robot. (**A**) The robot locomotion in a straight vessel. (**B**) The robot traverses a narrow segment. (**C**) The robot locomotion within a Y-shaped vessel phantom. The robot can return to the main vessel from one branch, and then enter another branch. (**D**) The locomotion of the robot within vessel phantoms with inclined branches. (**E**) The locomotion of the robot within a phantom with blood flow (10 mm/s) under ultrasound imaging. (**F**) The relationship between the robot speed and magnet rotating frequency. Data are presented as mean ± s.d. from three independent experiments (n = 3). Scale bars, 4 mm.

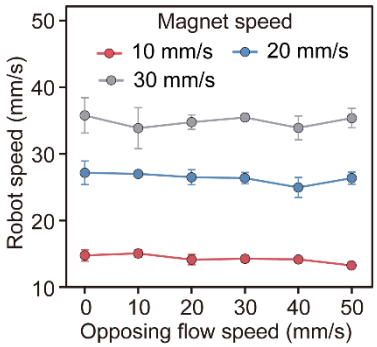

Fig. S14. The relationship of robot speed with the opposing flow speed under tumbling locomotion mode. Data are presented as mean ± s.d. from three independent experiments (n = 3).

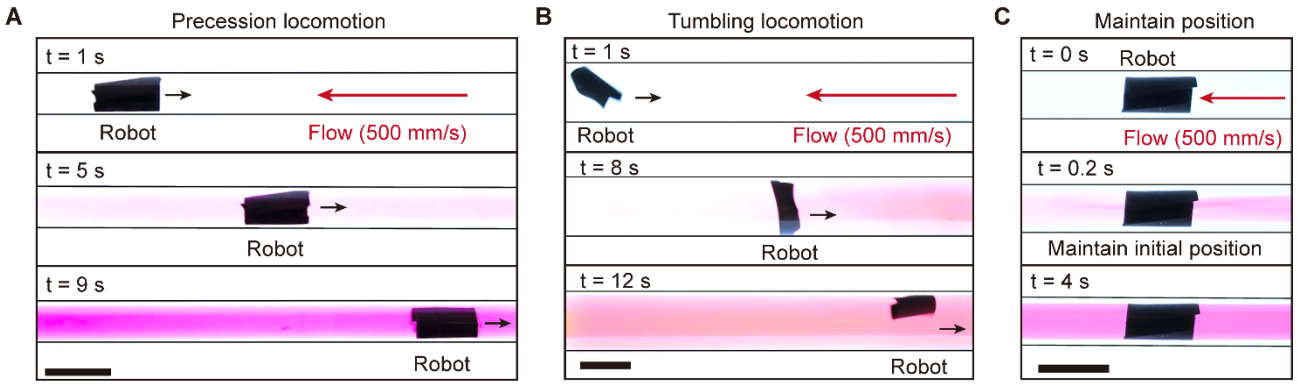

Fig. S15. Locomotion and anchoring of the robot under high-flow conditions. (**A**) Adaptive robot locomotion with precession motion in a narrow channel. Channel width: 4 mm. (**B**) Adaptive robot locomotion with tumbling motion in a wide channel. Channel width: 10 mm. (**C**) Anchoring capability of the robot in a channel. The channels in all trials are applied with a 500 mm/s flow. Scale bars, 10 mm.

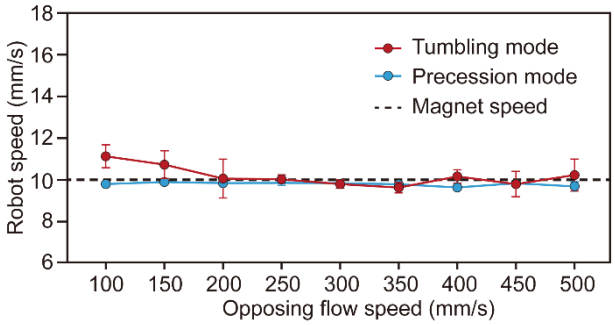

Fig. S16. The relationship between the robot moving speed with opposing flow speeds. The permanent magnet for actuation moves with a speed of 10 mm/s. Data are presented as mean ± s.d. from three independent experiments (n = 3). The diameter of the drive magnet is 100 mm, with a height of 50 mm.

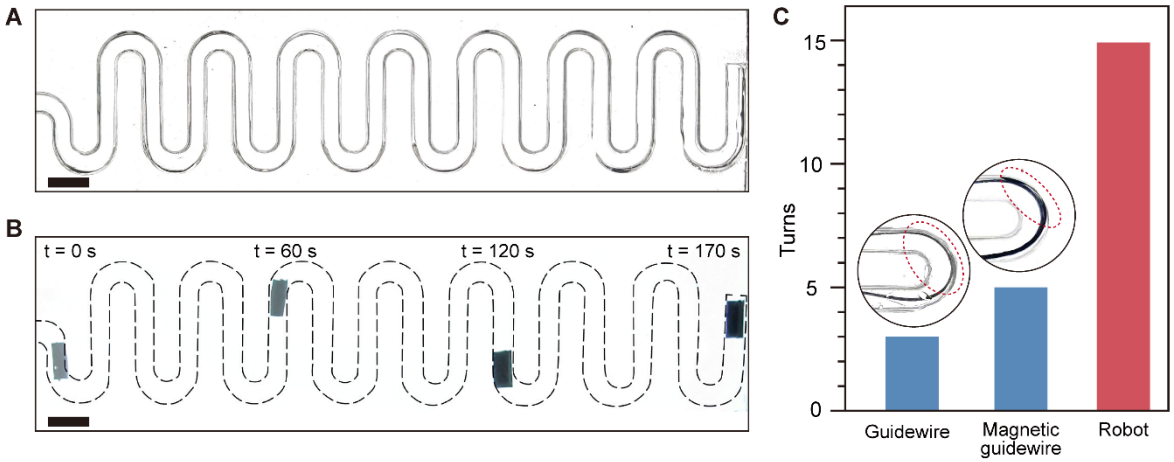

Fig. S17. Comparison on locomotion capability of the proposed robot, a clinically used guidewire and a magnetic guidewire in a tortuous environment. (**A**) The silicone vessel phantom with 15 U-shaped turns. (**B**) Locomotion of the robot in the vessel phantom. The robot can successfully pass through all turns. (**C**) Navigation of a clinically used guidewire and a magnetic guidewire in the phantom, which can pass through three turns and five turns, respectively. Scale bars, 10 mm.

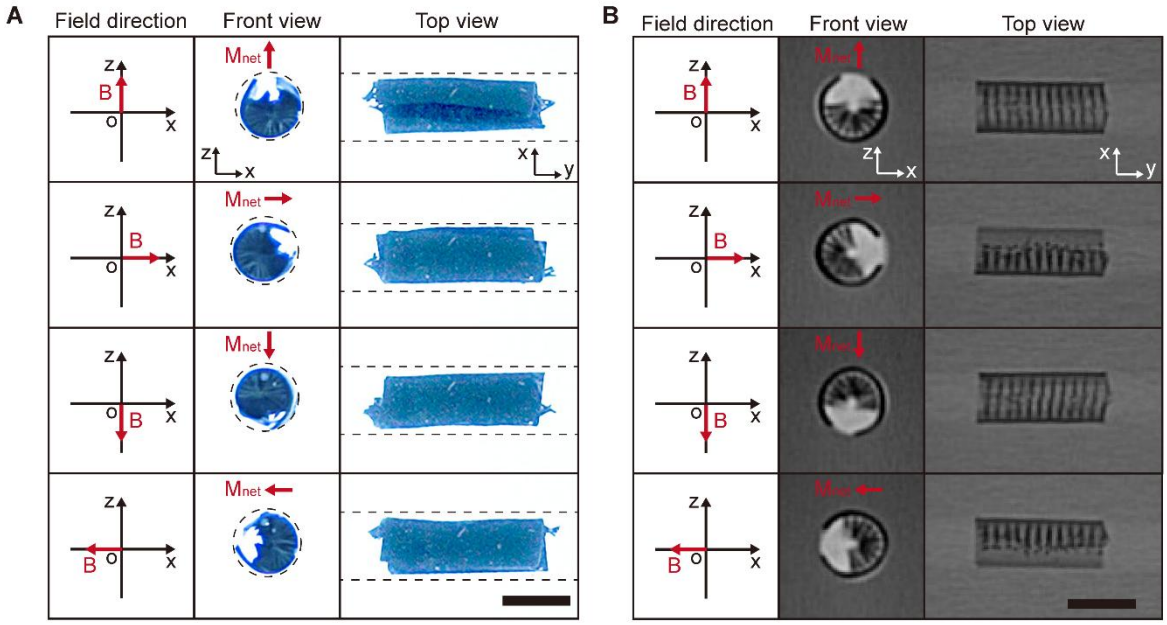

Fig. S18. Pose adjustment of the robot. (**A**) Pose tuning of the robot under magnetic fields in a tube. (**B**) Pose tuning of the robot using X-ray imaging feedback. Scale bars, 4 mm.

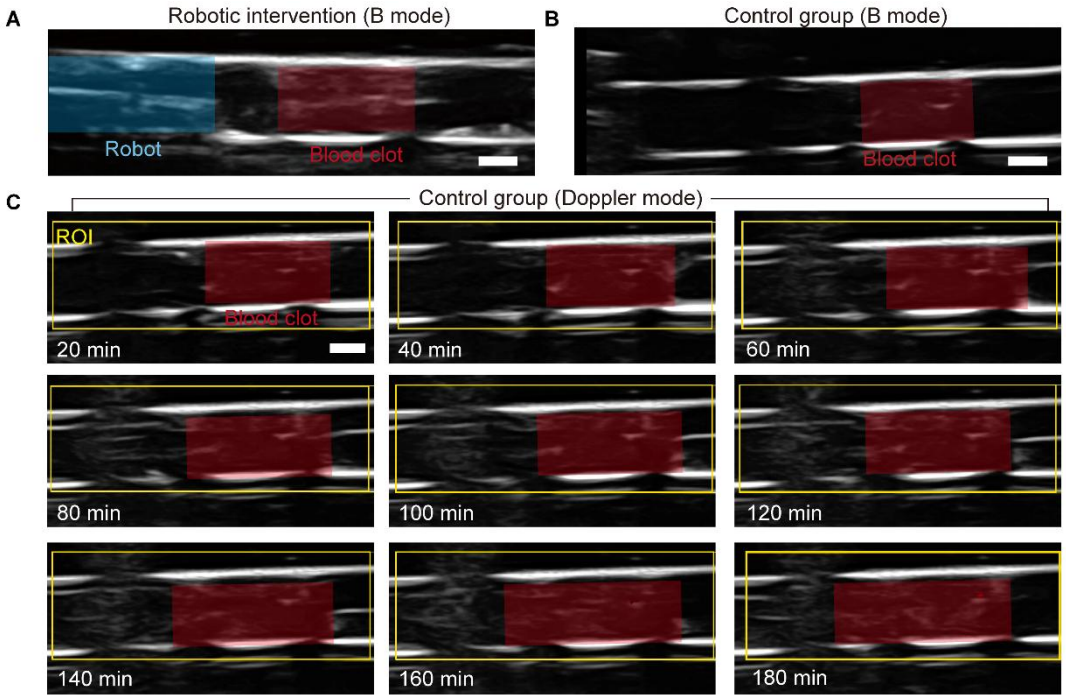

Fig. S19. In vitro thrombolysis validation within whole blood under ultrasound imaging. (**A**) The image of the group with robotic flow regulation under B mode imaging. Both the robot and the blood clot can be clearly observed. (**B**) The image of the group without robot under B mode imaging. The blood clot is clearly observed. (**C**) The whole in vitro process of the group without robot under Doppler imaging. No blood flow signal is observed. Scale bars, 2 mm.

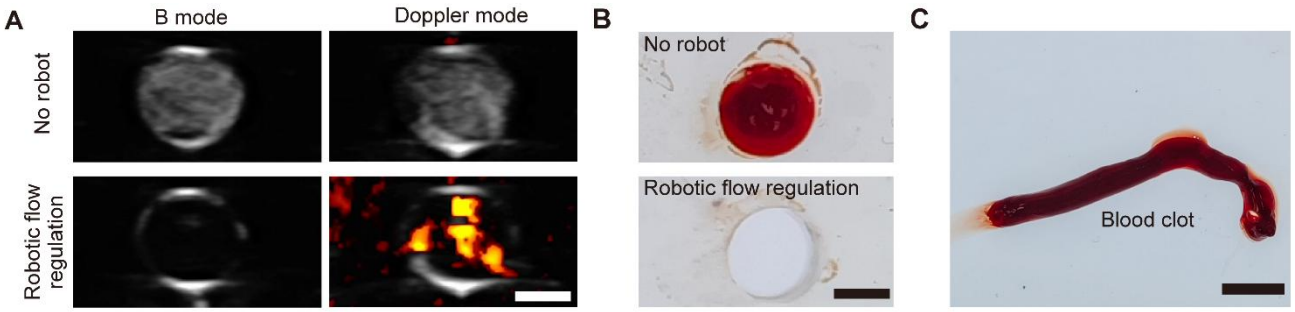

Fig. S20. Investigation of robot thrombogenicity in a blood flow loop. (**A**) Cross-sectional ultrasound imaging of the branches under B-mode and Doppler mode at 180 minutes. Scale bar, 2 mm. (**B**) The cross sections of two branches. Scale bar, 2 mm. (**C**) The thrombus formed in the branch without robot deployment. Scale bar, 4 mm. The flow speed in the main vessel is 4 mm/s in the experiment.

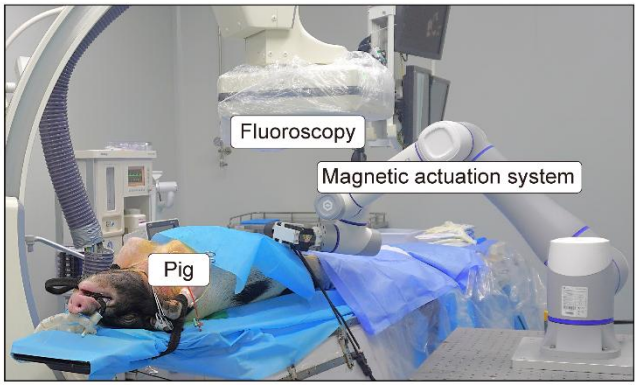

Fig. S21. Experimental setup for in vivo thrombolysis validation. A cylindrical magnet is mounted on a motor, which is attached to the robotic arm's end-effector for precise control of the robot. Real-time monitoring through C-arm X-ray imaging during the entire experimental procedure.

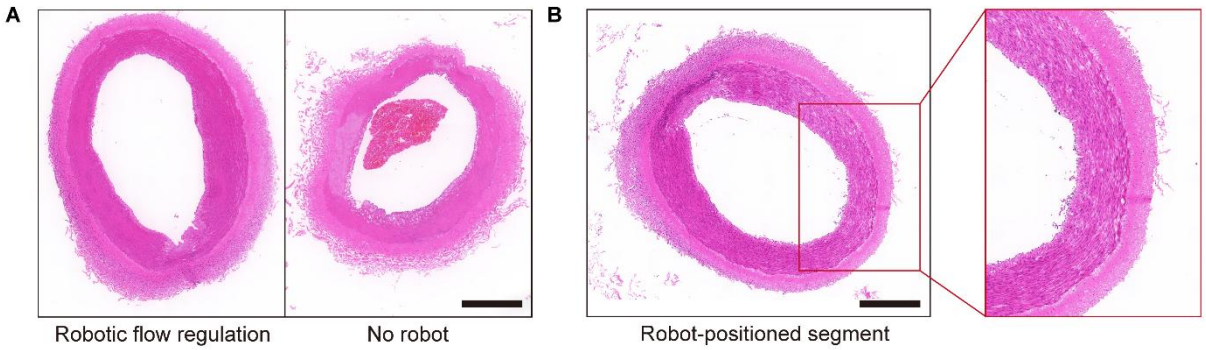

Fig. S22. The H&E staining cross-sectional images of the blood vessels in the in vivo thrombolysis experiment. (**A**) The H&E staining cross-sectional images of the residual thrombus. (**B**) The H&E staining cross-sectional images of the blood vessels surrounding the robot during the in vivo thrombolysis experiment. Scale bars, 400 μm.

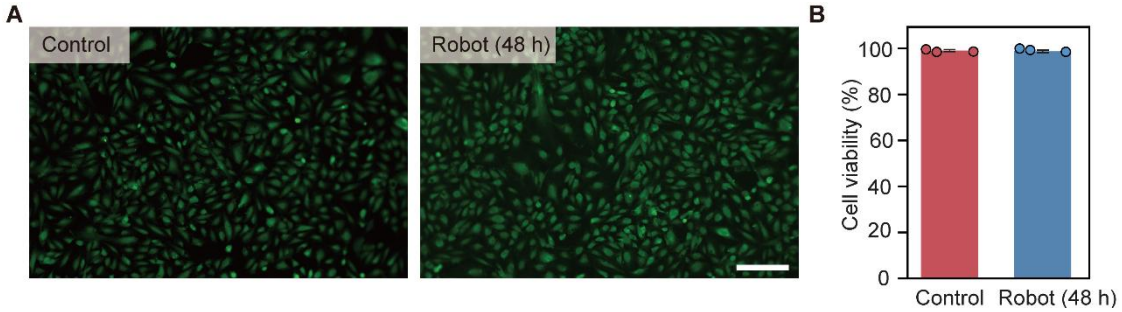

Fig. S23. Assessment of robot cytotoxicity. (**A**) Fluorescence microscopy images of HUVECs stained with a live-cell indicator after 48 hours of incubation with the robot compared to a control group. Scale bar, 200 µm. (**B**) Quantitative analysis of cell viability. Data are presented as mean ± s.d. from three independent experiments (n = 3).

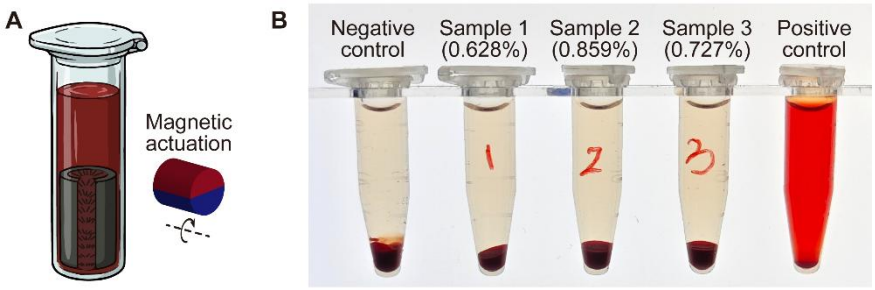

Fig. S24. Hemolysis evaluation of the robot. (**A**) Schematic illustration of the experimental procedure for the hemolysis assay. Centrifuge tube icon is created using Adobe Illustrator. (**B**) Red blood cell (RBC) suspensions after exposure to the actuated robot. PBS and deionized water serve as negative and positive controls, respectively.

Supporting Movies

Movie S1. Motion of a cilium
This movie demonstrates the motion of an axially magnetized cilium in a cycle at different field-cilium angles α, which is the angle between its long axis and the rotating plane of the magnetic field. The frequency of the applied rotating magnetic field is 0.5 Hz.

Movie S2. Wave propagation and fluid transportation of cilia carpets
This movie presents the wave propagation and fluid transportation of cilia carpets with the antiplectic wave and the symplectic wave, respectively.

Movie S3. In vitro flow regulation
This movie presents the active flow regulation capability of the robot in different vessel conditions, which include a fully occluded vessel, a narrowed vessel, and an unobstructed vessel. The vessels are filled with a glycerol-water mixture, matching the human blood viscosity.

Movie S4. In vitro locomotion, deployment and retrieval
This movie shows the multimodal locomotion and retrieval of the robot within blood vessel phantoms.

Movie S5. In vitro accelerated thrombolysis
This movie shows that robotic flow regulation is capable of accelerated thrombolysis.

Movie S6. In vitro accelerated thrombolysis in whole blood
This movie presents accelerated thrombolysis with robotic flow regulation in porcine whole blood, monitored by Doppler ultrasound imaging. No blood flow signal is observed when the robot is not actuated. When magnetic actuation is applied, blood flow signals emerge between the blood clot and the robot.

Movie S7. In vivo locomotion of a robot
This movie demonstrates the multimodal locomotion and retrieval of the robot within blood vessels. The robot can adapt its locomotion mode according to the vessel size. The robot can be magnetically navigated back to a catheter, and endovascular retrieval is achieved.

Movie S8. In vivo accelerated thrombolysis
This movie presents in vivo accelerated thrombolysis in porcine models. In the case of robotic flow regulation, the thrombus is completely dissolved, and complete recanalization is achieved as indicated by contrast agent injection. In the case without robotic flow regulation, no significant change of the thrombus before and after treatment, and the blood vessel is fully occluded after treatment.